

Unconventional Superconducting Quantum Criticality in Monolayer WTe₂

Tiancheng Song¹, Yanyu Jia¹, Guo Yu^{1,2}, Yue Tang¹, Pengjie Wang¹, Ratnadwip Singha³, Xin Gui³, Ayelet J. Uzan¹, Michael Onyszczak¹, Kenji Watanabe⁴, Takashi Taniguchi⁵, Robert J. Cava³, Leslie M. Schoop³, N. P. Ong¹, Sanfeng Wu^{1*}

¹Department of Physics, Princeton University, Princeton, New Jersey 08544, USA.

²Department of Electrical and Computer Engineering, Princeton University, Princeton, New Jersey 08544, USA.

³Department of Chemistry, Princeton University, Princeton, New Jersey 08544, USA.

⁴Research Center for Functional Materials, National Institute for Materials Science, 1-1 Namiki, Tsukuba 305-0044, Japan.

⁵International Center for Materials Nanoarchitectonics, National Institute for Materials Science, 1-1 Namiki, Tsukuba 305-0044, Japan.

*Correspondence to: sanfengw@princeton.edu

Abstract

The superconductor to insulator or metal transition in two dimensions (2D) provides a valuable platform for studying continuous quantum phase transitions (QPTs) and critical phenomena^{1,2}. Distinct theoretical models, including both fermionic and bosonic localization scenarios¹⁻³, have been developed, but many questions remain unsettled. The presence of an anomalous metal state near the transition in various systems further enriches the field and challenges existing theories². Using the Nernst effect, we uncover anomalous quantum fluctuations and identify an unconventional superconducting quantum critical point (QCP) in a gate-tuned excitonic quantum spin Hall insulator (QSHI)⁴⁻¹¹, the monolayer tungsten ditelluride (WTe₂). The observed vortex Nernst effect reveals singular superconducting fluctuations in the resistive normal state induced by magnetic fields or temperature, even well above the transition. Near the doping-induced QCP, the Nernst signal driven by quantum fluctuations is very large in the millikelvin regime, with a coefficient of $\sim 4,100 \mu\text{V}/\text{KT}$ at zero magnetic field, an indication of the proliferation of vortices. However, the Nernst signal abruptly disappears when the doping is decreased below the gate-tuned QPT, in striking conflict with expectations for a conventional QPT. Our findings establish a 2D model platform for studying unconventional superconducting QPTs and quantum critical matter.

Main Text

Monolayer WTe₂ is an excellent system for investigating the 2D superconducting QPT in a clean crystalline material with minimal disorder. Distinct from all previous systems studied experimentally, the insulating state of the monolayer is a QSHI⁴⁻⁶, where recent experiments and theories have shown evidence for an excitonic insulator phase at its charge neutrality point⁹⁻¹³. With electrostatic gating, superconductivity occurs in this 2D crystal above a very low critical carrier density^{7,8}, on the order of 10^{12} cm^{-2} . Existing theories suggest that its pairing mechanism could be topological¹⁴ or spin-triplet¹⁵. The nature of this low-density superconductivity and the intriguing superconductor-to-QSHI quantum transition is currently unknown.

Vortex Nernst effect in the monolayer

We examine the superconducting QPT in monolayer WTe₂ by measuring the Nernst effect. The Nernst experiment detects a transverse voltage in a material placed in a perpendicular magnetic field (B) when a thermal gradient is applied in the longitudinal direction (Fig. 1a). In the case of a type-II superconductor, a magnetic field generates vortices that carry quantized flux and entropy in the superfluid. A temperature gradient ($-\nabla T$) can then drive a flow of vortices, producing phase slippage that engenders a transverse electric field (E) due to the Josephson relation. Since its observation in cuprates^{16,17} above the critical temperature (T_c), the Nernst effect has been widely observed in various superconductors¹⁸. As a sensitive probe to vortices and superconducting fluctuations, it reveals critical information hidden from electrical transport.

To detect the monolayer Nernst effect, we employ the geometry shown in Fig. 1a. The monolayer WTe₂ is fully encapsulated between graphite/hexagonal boron nitride (hBN) stacks to avoid degradation and enable gate-dependent studies (see Methods and Extended Data Fig. 1). The carrier density in the monolayer is modified by gate voltages applied to the top (V_{tg}) and bottom (V_{bg}) graphite layers. The gate-induced carrier density is $n_g \equiv \epsilon_r \epsilon_0 (V_{tg}/d_{tg} + V_{bg}/d_{bg})/e$, where d_{tg} (d_{bg}), ϵ_r , ϵ_0 , and e denotes, respectively, the thickness of top (bottom) hBN dielectric, its relative dielectric constant, vacuum permittivity, and elementary charge. Key to the Nernst experiments are the two microheaters fabricated next to the monolayer, each being a thin narrow metal stripe (~ 200 nm wide, ~ 8 nm thick, and ~ 1 k Ω resistance). We employ a dual-heater measurement scheme^{19–22}, in which a low-frequency ($\omega \sim 13$ Hz) alternating current is applied to the two microheaters, with a 90° phase shift between them, to produce an alternating ∇T with minimal perturbation to the sample temperature (T). The Nernst voltage drop (V_N) across the two probes is detected at the frequency of 2ω . Unlike in previous thermoelectric measurements on 2D materials where the heater is typically located on the SiO₂/Si substrate^{23–25}, here we fabricate the heaters directly inside the van der Waals stack. This method, which produces a finite ∇T with minimal heater power (P_h) (see Methods and Extended Data Figs. 2–4), enables Nernst measurements at millikelvin temperatures. Our approach can be universally applied to study the thermoelectricity of various 2D crystals and moiré materials.

Figure 1b depicts the electronic phase diagram of the monolayer, based on four-probe resistance (R_{xx}) taken on the same device (device 1) (Extended Data Fig. 5). Consistent with previous reports^{7,8}, it clearly shows both the superconducting and QSHI states with a critical carrier density, $n_{c,R} \sim 6.3 \times 10^{12}$ cm⁻², at which dR_{xx}/dT switches its sign. We characterize this gate-tuned 2D superconductor by the Berezinskii–Kosterlitz–Thouless (BKT) transition temperature (T_{BKT}), at which thermal fluctuations unbind vortex-antivortex pairs and produce a finite resistance. For each n_g well above $n_{c,R}$, we extract the corresponding T_{BKT} from its I - V characteristics following the usual procedure²⁶ (Extended Data Fig. 6). T_{BKT} , represented by the white dots in Fig. 1b, decreases monotonically with decreasing n_g and vanishes at a density slightly higher than $n_{c,R}$, signifying the n_g -tuned QPT.

We first present the Nernst data taken in the highly electron-doped regime ($n_g \sim 2.3 \times 10^{13}$ cm⁻²), where the highest T_c is observed. Figure 1c plots the Nernst signal (V_N) together with R_{xx} as a function of B , where V_N clearly develops a peak at the field-induced transition to the normal state

and vanishes near zero B (i.e., the vortex solid state) as well as at high B . With increasing T to high values, V_N disappears (Figs. 1d and e). The Nernst signal, which is antisymmetric with respect to B and coincides with the change in R_{xx} , directly probes the motion of vortices in the vortex liquid state^{17,18,27}. We further note that the absence of V_N at high B and high T implies that the quasiparticle contributions to the Nernst signal are negligible in our measurements.

Large quantum fluctuations in the underdoped regime

Our key results are shown in Fig. 2a, where the Nernst signal is recorded at $T \sim 45$ mK as a function of n_g , which is continuously tuned across the superconductor-to-QSHI transition. We discuss important findings near the n_g -tuned QPT in three regimes. The first one is the large Nernst signal observed in the underdoped regime at unexpectedly high B (labeled as “I” in Fig. 2a). In Fig. 2b, we present R_{xx} map measured under the same condition, where the black dotted line represents $B_{R,90\%}$, at which R_{xx} drops to 90% of its saturated value at high B (Extended Data Fig. 5). The same dotted line is also plotted in Fig. 2a. Substantial V_N is observed in regime I, well above $B_{R,90\%}$, despite that the R_{xx} data appears to suggest a normal resistive state with no hint of superconductivity. The Nernst data implies that there is a critical field, $B_{c,N}$, above which V_N vanishes (the white dashed line in Fig. 2c). Figures 2c & d highlight the gate dependence of $B_{c,N}$. In contrast to $B_{R,90\%}$, $B_{c,N}$ increases rapidly with decreasing n_g to the critical doping, where $B_{c,N}$, at least ~ 500 mT, is more than ten times higher than the corresponding $B_{R,90\%}$. Fig. 2e highlights the heater-power effect on V_N . The implications of these observations will be further discussed below.

The prominent Nernst signal in the underdoped regime is enhanced at the lowest T . Figure 2f plots the T -dependent V_N , together with R_{xx} , at $n_g \sim 7.0 \times 10^{12} \text{ cm}^{-2}$. At this doping, the zero-field R_{xx} displays only a slight drop below ~ 200 mK but doesn’t reach zero. At a B field of 150 mT, this low- T drop is completely suppressed, and an upturn is instead observed. Surprisingly, V_N at this B field remains substantial and survives to temperatures as high as ~ 700 mK (Fig. 2f), where traces of superconductivity in R_{xx} vanish at all dopings in this device (Fig. 1b). The Nernst signal above T_c was first observed in cuprates, indicating vortex-like excitations in the pseudogap regime^{16,17}. Our observation here occurs in the quantum regime. Figure 2f shows that V_N increases strongly with decreasing T . By extrapolation, the Nernst signal is finite in the limit of zero kelvin. It thus arises from quantum fluctuations, instead of thermal fluctuations.

Giant Nernst effect at the QCP and its sudden death

Remarkably, Fig. 2a clearly reveals a continuous evolution from the vortex liquid regime at high electron doping to the strongly quantum fluctuating regime near the n_g -tuned QPT in a single device. Sharply located at the QPT (labeled as “II” in Fig. 2a), the quantum fluctuation produces a giant Nernst signal near zero B , which is another key finding. In Fig. 3a, we carefully examine this regime by plotting V_N under very small B . One immediately observes that the Nernst signal is extremely sensitive to the QPT, i.e., a slight detuning of n_g away from $n_{\text{max}} \sim 7.2 \times 10^{12} \text{ cm}^{-2}$, where V_N is maximized, completely suppresses the signal on both sides. To demonstrate that this signal reflects the zero- B property of the QCP, we plot V_N/B in Fig. 3b (only the positive- B side is shown), which may be interpreted as the mobility of the vortices and shows a strong enhancement when B is reduced to near zero. Figure 3c further plots V_N versus B curves at selected n_g , in which we confirm that the largest slope occurs at n_{max} near zero B . In Methods, we estimate ∇T to be ~ 5.3

mK/ μm , based on which we obtain the corresponding Nernst coefficient, $\nu \equiv (dE/dB)/\sqrt{T}|_{B=0}$, to be $\sim 4,100 \mu\text{V}/\text{KT}$, an exceptionally high value. As a comparison, this giant Nernst coefficient is at least one order of magnitude higher than the typical ν measured in other superconductors^{17,18,27,28}. This large Nernst response near zero B indicates the proliferation of vortices and antivortices when the doping is reduced to the critical value.

The large Nernst signal abruptly disappears right below $n_{c,R} \sim 6.3 \times 10^{12} \text{ cm}^{-2}$ (labeled as ‘‘III’’ in Fig. 2a, and also in Figs. 3a & b). While the vanishing of V_N above n_{max} is expected in the vortex solid state, its sudden death right below $n_{c,R}$ is a surprise. As a comparison, previous studies in disordered superconducting films have reported substantial Nernst signal deep inside the insulating phase after the transition²⁸, in clear contrast to the monolayer WTe₂. Note that the noisy data that appears below $\sim 3.4 \times 10^{12} \text{ cm}^{-2}$ in Figs. 2a & 3a is not antisymmetric in B and hence not a Nernst signal (they likely arise due to bad contacts in the more insulating state). The absence of a Nernst signal in regime III is intrinsic, rather than a consequence of resolution limitations in the experiments. This can be seen in Fig. 2e, which reveals a clear contrast in the heater-power dependence of V_N between regimes III and I’, and demonstrates that V_N is invariably absent in regime III despite the 10-fold increase in heater power. This is true at all magnetic fields up to 500 mT (see Figs. 2c & d). Regime III is also anomalous in electrical transport. Figure 3d plots R_{xx} , where n_{max} and $n_{c,R}$ are both indicated by the red dashed lines. One finds that while R_{xx} displays a dramatic T dependence on the superconducting side, its value in regime III, on the order of $\sim \text{k}\Omega$, displays little changes with T . This indicates that a metallic-like state may reside right below $n_{c,R}$, before the QSHI/excitonic insulator^{6,9,10} is fully developed. The sudden death of V_N implies no superconducting fluctuations in the metallic-like state directly abutting the QPT.

These highly reproducible findings (see Extended Data Fig. 7 for the data taken from device 2) highlight the intriguing nature of the n_g -tuned QPT in monolayer WTe₂. To reinforce that the Nernst signal reflects the superconducting quantum fluctuations, in Fig. 4a, we plot the T -dependent V_N , taken at a fixed small B (2 mT). The amplitude of the signal increases rapidly when T is lowered, suggesting that the Nernst coefficient (ν) attains its maximum at zero kelvin. The corresponding n_{max} shifts its values at different T , which traces precisely the T_{BKT} determined from the transport measurement (the same as Fig. 1b). In the canonical phase diagram of a QPT, sketched in the inset of Fig. 4a, the BKT transition traces down to the QCP at absolute zero. The Nernst signal hence directly detects the superconducting QCP in the monolayer. Clearly, quantum fluctuations at the QCP produce the dramatic Nernst signal at the lowest T .

Discussion

We next highlight observations that challenge the conventional wisdom on QPTs. The standard Landau-Ginzburg-Wilson (LGW) theory²⁹ describes a continuous transition between an ordered state and a ‘‘disordered’’ state. The order parameter fluctuations are expected to be stronger on the ‘‘disordered’’ side reflecting suppression of phase fluctuations on the ordered side. In a superconducting transition, a pronounced fluctuation tail penetrating into the normal state is expected and may be further enhanced in the presence of a vortex liquid state above the transition, as widely seen in cuprates¹⁷. Such conventional expectations of order parameter fluctuations are general, independent of the tuning parameter used for inducing the transition.

In our experiment, we observed three types of superconducting phase transitions in a single device: (a) the T -tuned transition; (b) the B -tuned transition; and (c) the n_g -tuned transition. Indeed, both (a) and (b) follow the above conventional expectations, i.e., pronounced Nernst signals are seen in the normal states (see, e.g., Fig. 2f for the T -tuned transition and Figs. 2a & c for the B -tuned transition). However, the transition of (c), the n_g -tuned QPT, is strikingly different. The sudden death of the Nernst signal in the normal state below the critical doping n_c (regime III in Fig. 2a) is anomalous, and not anticipated at all in the conventional scenario. We conclude that the n_g -tuned superconducting QCP in monolayer WTe₂ is unconventional.

We further summarize the key experimental features related to this unconventional QCP in Fig. 4b. In the regime $n_g > n_c$, $B_{c,N}$ provides a measure of the pairing strength in the superconducting state. The increase of $B_{c,N}$ implies that the pairing strength increases monotonically as $n_g \rightarrow n_c^+$ (Fig. 4b upper panel), an unexpected behavior. Paradoxically, in spite of the increasing pairing strength, V_N vanishes abruptly once n_g is decreased below n_c (sudden death). One possible way to explain the sudden death is to assume that a new ordered phase emerges in the regime $n_g < n_c$. This is suggested by the fluctuations in the following two limits. In the limit of $B \rightarrow 0$ and $T \rightarrow 0$ (Fig. 4b middle panel), the giant Nernst response observed at n_c separates two distinct phases with no detectable fluctuations on either side. On the right side, this is understood because the pairing leads to an ordered superconducting state. It is however challenging to explain the absence of fluctuations on the left side if it is treated as a usual metallic-like state. As a comparison, in the limit of large B and $T \rightarrow 0$ (Fig. 4b lower panel), the right side is now in a normal metal state (above $B_{c,N}$). Reducing $n_g \rightarrow n_c^+$, strong Nernst signal occurs and signifies the fluctuations, with a long tail appearing on the right metallic side. This is in sharp contrast to the sudden death of V_N on the left side, even though it displays a similar metallic resistivity. The highly asymmetric fluctuations (the lower panel) seem to suggest a transition from the normal metallic phase (above n_c) to an ordered phase (below n_c) that does not superconduct. Note that the phase below n_c arises from doping electrons into the excitonic QSHI, which might be an important clue for uncovering its nature. Interestingly, the possibility of a “deconfined” QCP^{30,31}, which goes beyond the LGW paradigm and separates two distinct ordered phases, has been explored theoretically at the superconducting transition induced by doping a QSHI^{32–34} (see Methods for further discussions).

There is strong interest in searching for systems hosting an unconventional QCP that violates the standard LGW description^{30–40}, but their experimental detection is difficult. Several other 2D systems have also shown interesting quantum criticality^{41–44}, where the physics is distinct from the case reported here. Our experiment shows that, in general, fluctuations in the vicinity of a QCP provide a powerful probe to the nature of a QPT.

References

1. Goldman, A. M. & Marković, N. Superconductor-Insulator Transitions in the Two-Dimensional Limit. *Phys Today* **51**, 39–44 (1998).
2. Kapitulnik, A., Kivelson, S. A. & Spivak, B. Colloquium: Anomalous metals: Failed superconductors. *Rev. Mod. Phys.* **91**, 011002 (2019).
3. Lin, Y.-H., Nelson, J. & Goldman, A. M. Superconductivity of very thin films: The superconductor–insulator transition. *Phys. C Supercond. Appl.* **514**, 130–141 (2015).

4. Qian, X., Liu, J., Fu, L. & Li, J. Quantum spin Hall effect in two-dimensional transition metal dichalcogenides. *Science* **346**, 1344–1347 (2014).
5. Fei, Z. *et al.* Edge conduction in monolayer WTe₂. *Nat. Phys.* **13**, 677–682 (2017).
6. Wu, S. *et al.* Observation of the quantum spin Hall effect up to 100 kelvin in a monolayer crystal. *Science* **359**, 76–79 (2018).
7. Fatemi, V. *et al.* Electrically tunable low-density superconductivity in a monolayer topological insulator. *Science* **362**, eaar4642 (2018).
8. Sajadi, E. *et al.* Gate-induced superconductivity in a monolayer topological insulator. *Science* **362**, eaar4426 (2018).
9. Wang, P. *et al.* Landau quantization and highly mobile fermions in an insulator. *Nature* **589**, 225–229 (2021).
10. Jia, Y. *et al.* Evidence for a monolayer excitonic insulator. *Nat. Phys.* **18**, 87–93 (2022).
11. Sun, B. *et al.* Evidence for equilibrium exciton condensation in monolayer WTe₂. *Nat. Phys.* **18**, 94–99 (2022).
12. Lee, P. A. Quantum oscillations in the activated conductivity in excitonic insulators: Possible application to monolayer WTe₂. *Phys. Rev. B.* **103**, L041101 (2021).
13. Kwan, Y. H., Devakul, T., Sondhi, S. L. & Parameswaran, S. A. Theory of competing excitonic orders in insulating WTe₂ monolayers. *Phys. Rev. B.* **104**, 125133 (2021).
14. Hsu, Y.-T., Cole, W. S., Zhang, R.-X. & Sau, J. D. Inversion-Protected Higher-Order Topological Superconductivity in Monolayer WTe₂. *Phys. Rev. Lett.* **125**, 097001 (2020).
15. Crépel, V. & Fu, L. Spin-triplet superconductivity from excitonic effect in doped insulators. *Proc. Natl. Acad. Sci.* **119**, e2117735119 (2022).
16. Xu, Z. A., Ong, N. P., Wang, Y., Kakeshita, T. & Uchida, S. Vortex-like excitations and the onset of superconducting phase fluctuation in underdoped La_{2-x}Sr_xCuO₄. *Nature* **406**, 486–488 (2000).
17. Wang, Y., Li, L. & Ong, N. P. Nernst effect in high-T_c superconductors. *Phys. Rev. B.* **73**, 024510 (2006).
18. Rischau, C. W. *et al.* Universal Bound to the Amplitude of the Vortex Nernst Signal in Superconductors. *Phys. Rev. Lett.* **126**, 077001 (2021).
19. Aubin, M., Ghamlouch, H. & Fournier, P. Measurement of the Seebeck coefficient by an ac technique: Application to high-temperature superconductors. *Rev. Sci. Instrum.* **64**, 2938–2941 (1993).
20. Resel, R. *et al.* Thermopower measurements in magnetic fields up to 17 tesla using the toggled heating method. *Rev. Sci. Instrum.* **67**, 1970–1975 (1996).
21. Choi, E. S., Brooks, J. S., Qualls, J. S. & Song, Y. S. Low-frequency method for magnetothermopower and Nernst effect measurements on single crystal samples at low temperatures and high magnetic fields. *Rev. Sci. Instrum.* **72**, 2392–2397 (2001).
22. Li, X.-Q., Li, Z.-L., Zhao, J.-J. & Wu, X.-S. Electrical and thermoelectric study of two-dimensional crystal of NbSe₂. *Chinese Phys. B.* **29**, 087402 (2020).
23. Zuev, Y. M., Chang, W. & Kim, P. Thermoelectric and Magnetothermoelectric Transport Measurements of Graphene. *Phys. Rev. Lett.* **102**, 096807 (2009).
24. Checkelsky, J. G. & Ong, N. P. Thermopower and Nernst effect in graphene in a magnetic field. *Phys. Rev. B.* **80**, 081413(R) (2009).

25. Wei, P., Bao, W., Pu, Y., Lau, C. N. & Shi, J. Anomalous Thermoelectric Transport of Dirac Particles in Graphene. *Phys. Rev. Lett.* **102**, 166808 (2008).
26. Saito, Y., Nojima, T. & Iwasa, Y. Highly crystalline 2D superconductors. *Nat. Rev. Mater.* **2**, 16094 (2016).
27. Ienaga, K., Hayashi, T., Tamoto, Y., Kaneko, S. & Okuma, S. Quantum Criticality inside the Anomalous Metallic State of a Disordered Superconducting Thin Film. *Phys. Rev. Lett.* **125**, 257001 (2020).
28. Roy, A., Shimshoni, E. & Frydman, A. Quantum Criticality at the Superconductor-Insulator Transition Probed by the Nernst Effect. *Phys. Rev. Lett.* **121**, 047003 (2018).
29. Sachdev, S. Quantum Phase Transitions, 2nd ed. (Cambridge University Press, Cambridge, England, 2011).
30. Senthil, T., Vishwanath, A., Balents, L., Sachdev, S. & Fisher, M. P. A. Deconfined Quantum Critical Points. *Science* **303**, 1490–1494 (2004).
31. Sandvik, A. W. Evidence for Deconfined Quantum Criticality in a Two-Dimensional Heisenberg Model with Four-Spin Interactions. *Phys. Rev. Lett.* **98**, 227202 (2007).
32. Grover, T. & Senthil, T. Topological Spin Hall States, Charged Skyrmions, and Superconductivity in Two Dimensions. *Phys. Rev. Lett.* **100**, 156804 (2008).
33. Liu, Y. *et al.* Superconductivity from the condensation of topological defects in a quantum spin-Hall insulator. *Nat. Commun.* **10**, 2658 (2019).
34. Wang, Z. *et al.* Doping-Induced Quantum Spin Hall Insulator to Superconductor Transition. *Phys. Rev. Lett.* **126**, 205701 (2021).
35. Christos, M., Sachdev, S. & Scheurer, M. S. Superconductivity, correlated insulators, and Wess–Zumino–Witten terms in twisted bilayer graphene. *Proc. National Acad. Sci.* **117**, 29543–29554 (2020).
36. Khalaf, E., Chatterjee, S., Bultinck, N., Zaletel, M. P. & Vishwanath, A. Charged skyrmions and topological origin of superconductivity in magic-angle graphene. *Sci. Adv.* **7** : eabf5299 (2021).
37. Lee, J. Y., You, Y.-Z., Sachdev, S. & Vishwanath, A. Signatures of a Deconfined Phase Transition on the Shastry-Sutherland Lattice: Applications to Quantum Critical $\text{SrCu}_2(\text{BO}_3)_2$. *Phys. Rev. X* **9**, 041037 (2019).
38. Guo, J. *et al.* Quantum Phases of $\text{SrCu}_2(\text{BO}_3)_2$ from High-Pressure Thermodynamics. *Phys. Rev. Lett.* **124**, 206602 (2020).
39. Jiménez, J. L. *et al.* A quantum magnetic analogue to the critical point of water. *Nature* **592**, 370–375 (2021).
40. Cui, Y. *et al.* Proximate deconfined quantum critical point in $\text{SrCu}_2(\text{BO}_3)_2$. arXiv:2204.08133v2 (2022).
41. Yang, C. *et al.* Intermediate bosonic metallic state in the superconductor-insulator transition. *Science* **366**, 1505–1509 (2019).
42. Ghiotto, A. *et al.* Quantum criticality in twisted transition metal dichalcogenides. *Nature* **597**, 345–349 (2021).
43. Li, Q. *et al.* Tunable quantum criticalities in an isospin extended Hubbard model simulator. *Nature* **609**, 479–484 (2022).
44. Jaoui, A. *et al.* Quantum critical behaviour in magic-angle twisted bilayer graphene. *Nat. Phys.* **18**, 633–638 (2022).

45. Wang, P. *et al.* Piezo-driven sample rotation system with ultra-low electron temperature. *Rev. Sci. Instrum.* **90**, 023905 (2019).

Acknowledgments

We acknowledge helpful discussions with Z. Bi, T. Grover, F. D. M. Haldane, D. Huse, B. Lian, S. Ryu, S. Sondhi, A. Vishwanath, A. Yazdani and Y. Zhang. We especially thank L. Pfeiffer and M. Shayegen for their GaAs sample, which was used for calibrating the electron temperature of our dilution refrigerator. This work is mainly supported by ONR through a Young Investigator Award (N00014-21-1-2804) to S.W. Measurement systems and data collection are partially supported by NSF through a CAREER award (DMR-1942942) to S.W. N.P.O. is supported by the U.S. Department of Energy (DE-SC0017863). S.W. and L.M.S. acknowledge support from the Eric and Wendy Schmidt Transformative Technology Fund at Princeton. Materials synthesis and device fabrication are partially supported by the Materials Research Science and Engineering Center (MRSEC) program of the National Science Foundation (DMR-2011750) through support to R.J.C., L.M.S., N.P.O., and S.W. T.S. acknowledges support from the Princeton Physics Dicke Fellowship program. A.J.U. acknowledges support from the Rothschild Foundation and the Zuckerman Foundation. K.W. and T.T. acknowledge support from the JSPS KAKENHI (Grant Numbers 19H05790, 20H00354, and 21H05233). L.M.S. and N.P.O. acknowledge support from the Gordon and Betty Moore Foundation through Grants GBMF9064 and GBMF9466, respectively. L.M.S. is also supported by the David and Lucile Packard Foundation and the Sloan Foundation.

Author contributions

S.W. designed the project. T.S. fabricated the devices and performed measurements, assisted by Y.J., Y.T., G.Y., P.W., A.J.U., and M.O. G.Y. and P.W. built the dilution refrigerator measurement system. T.S., S.W., and N.P.O. analyzed the data. R.S., L.M.S., X.G., and R.J.C. grew and characterized bulk WTe_2 crystals. K.W. and T.T. provided hBN crystals. S.W., T.S., and N.P.O. interpreted the results and wrote the paper with input from all authors.

Competing interests

The authors declare that they have no competing interests.

Data availability

All data needed to evaluate the conclusions in the paper are presented in the paper. Additional data related to this paper are available from the corresponding author upon reasonable request.

Fig. 1

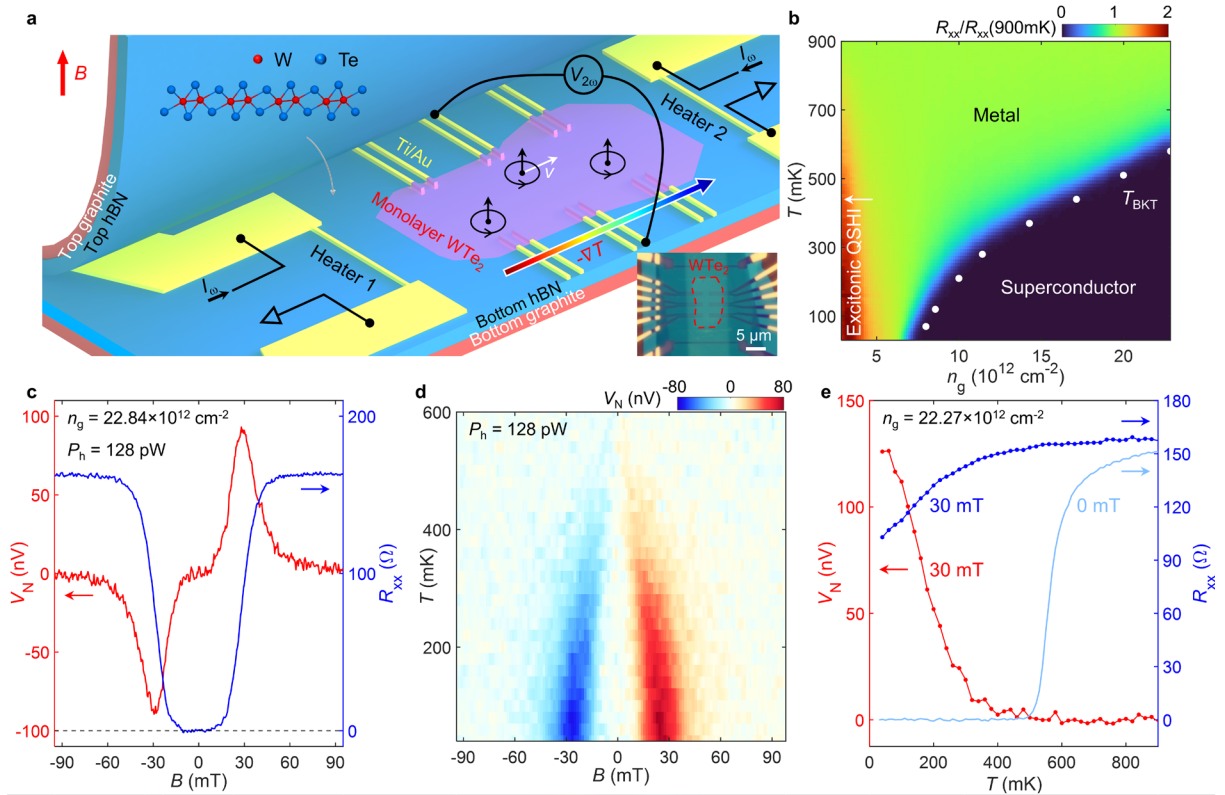


Fig. 1 | Vortex Nernst effect and electronic phase diagram of monolayer WTe_2 . **a**, Cartoon illustration of the device structure for measuring Nernst signal. Current is applied to the two microheaters to produce a temperature gradient on the monolayer WTe_2 . The inset shows the optical microscope image of device 1. The monolayer WTe_2 flake is outlined in red. **b**, Four-probe resistance as a function of n_g and T , measured on the same device. For each n_g , R_{xx} is normalized to its value at 900 mK to highlight its temperature dependence (also see Extended Data Fig. 5). The white dots represent T_{BKT} . **c**, Nernst signal (red) and R_{xx} (blue) as a function of magnetic field (B) for $n_g = 22.84 \times 10^{12} \text{ cm}^{-2}$. The dual-heater power (P_h) is 128 pW. **d**, B -dependence of V_N as a function of T for the same n_g . **e**, T -dependence of V_N (red) and R_{xx} (blue) measured at 30 mT for $n_g = 22.27 \times 10^{12} \text{ cm}^{-2}$. The zero-field R_{xx} is shown as a reference (light blue).

Fig. 2

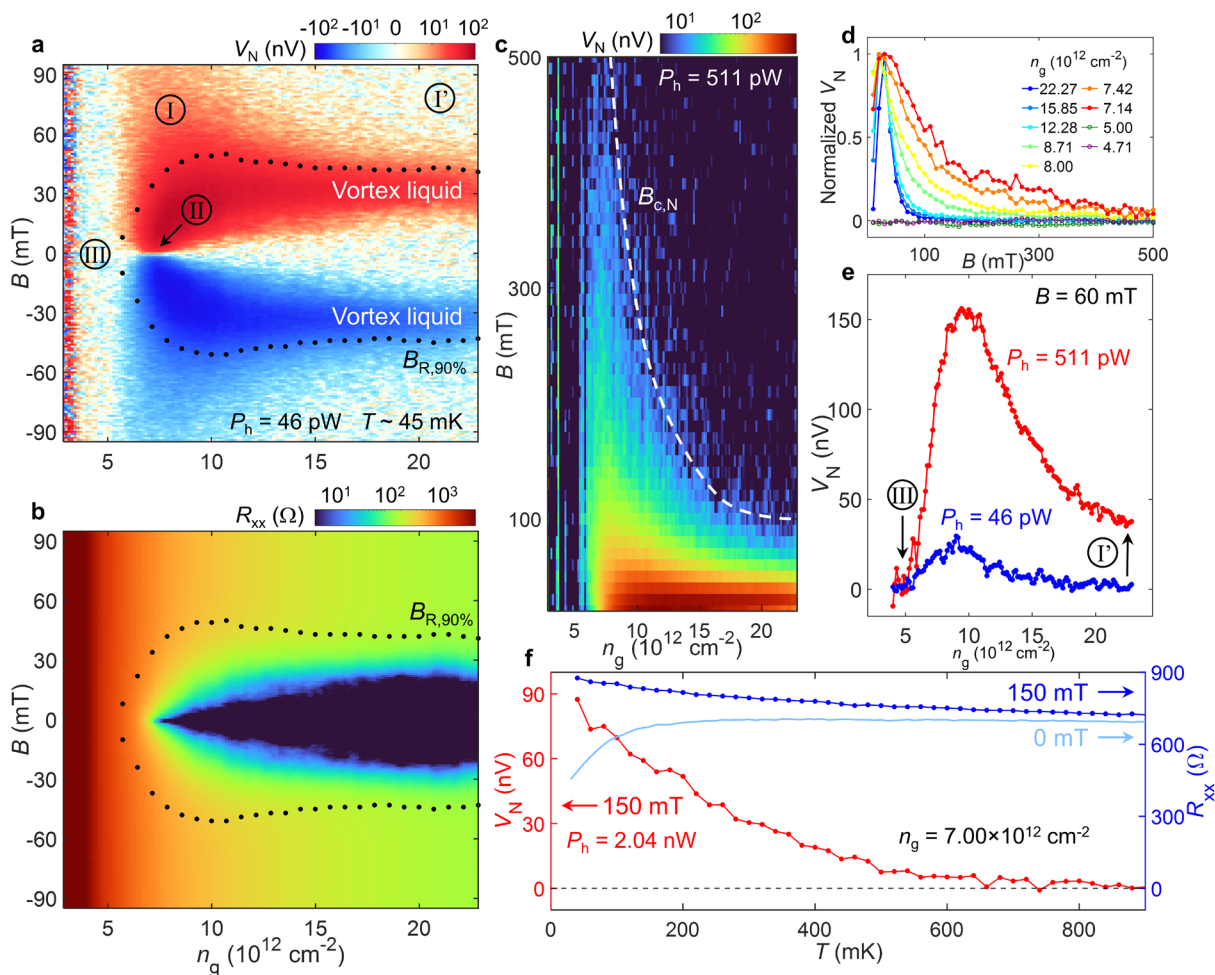


Fig. 2 | Gate-tuned Nernst effect and superconducting fluctuations well above critical magnetic field and critical temperature. **a**, Nernst signal as a function of n_g and B . Three different regimes of interest are labeled as I, II, III, respectively. **b**, R_{xx} as a function of n_g and B measured under the same condition as **a**. The black dotted line represents $B_{R,90\%}$, at which R_{xx} drops to 90% of its saturated value at high B . **c**, Nernst signal measured up to high B , with a higher power ($P_h = 511$ pW). The white dashed line indicates the critical field, $B_{c,N}$, above which V_N vanishes. **d**, n_g -dependence of the Nernst signal versus B . V_N is normalized to its peak value. **e**, Heater-power effect on the Nernst signal. The data are horizontal line cuts of **a** and **c**, respectively, at $B = 60$ mT. **f**, T -dependence of V_N (red) and R_{xx} (blue) measured at 150 mT for a selected low density near the QPT ($n_g = 7.00 \times 10^{12}$ cm $^{-2}$). The zero-field R_{xx} is shown as a reference (light blue).

Fig. 3

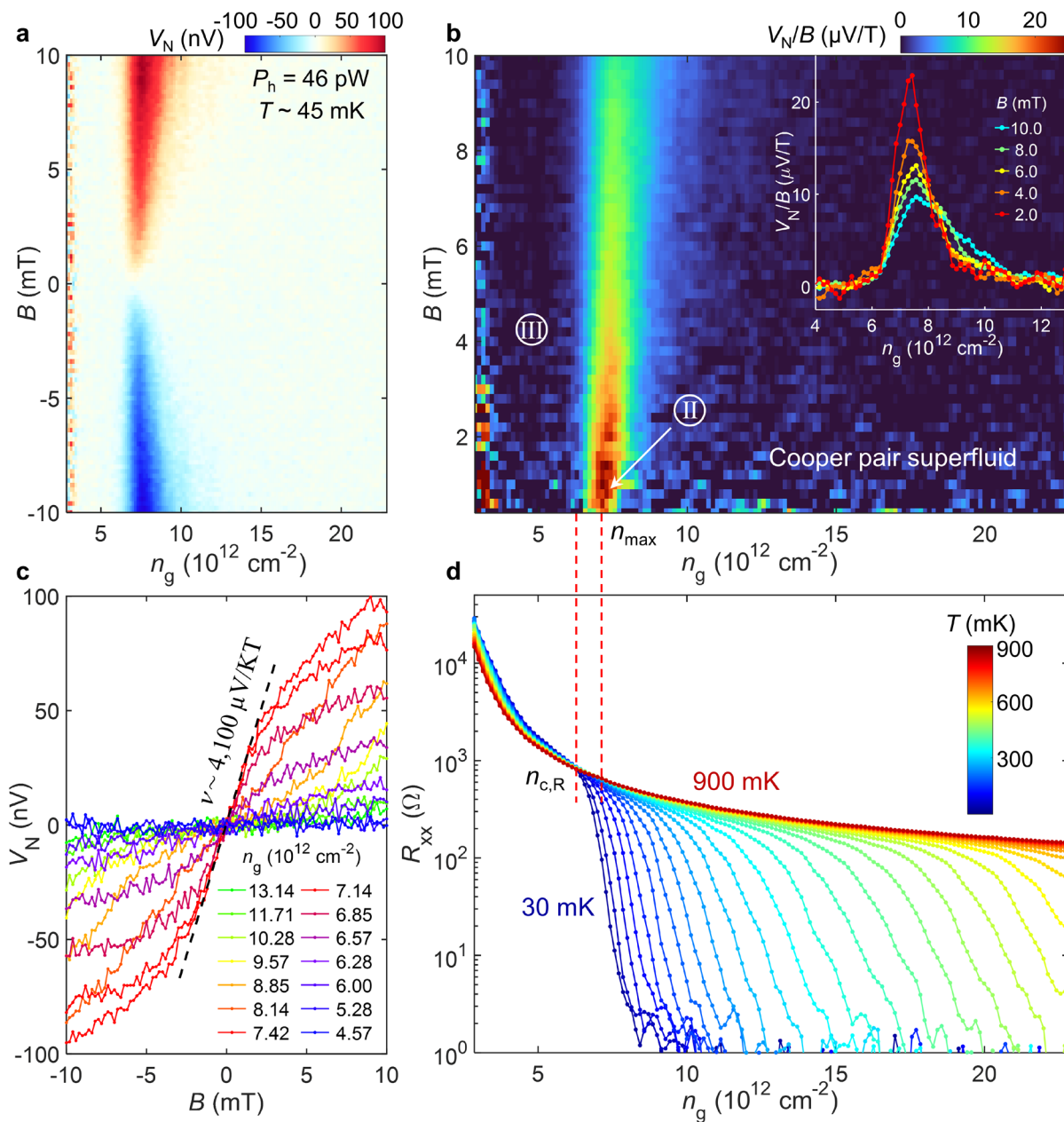


Fig. 3 | Giant Nernst effect at the QCP and its sudden death. **a**, Nernst signal as a function of n_g under very small B . **b**, V_N/B as a function of n_g and B , calculated from **a**. Only the positive- B side is shown. Inset displays selected line cuts of the same data. **c**, V_N versus B curves at selected n_g . The dashed line extracts the largest slope, which occurs at n_{max} near zero B . The estimated ν is indicated. **d**, T -dependence of R_{xx} versus n_g . The two red dashed lines indicate $n_{c,R}$ and n_{max} , respectively.

Fig. 4

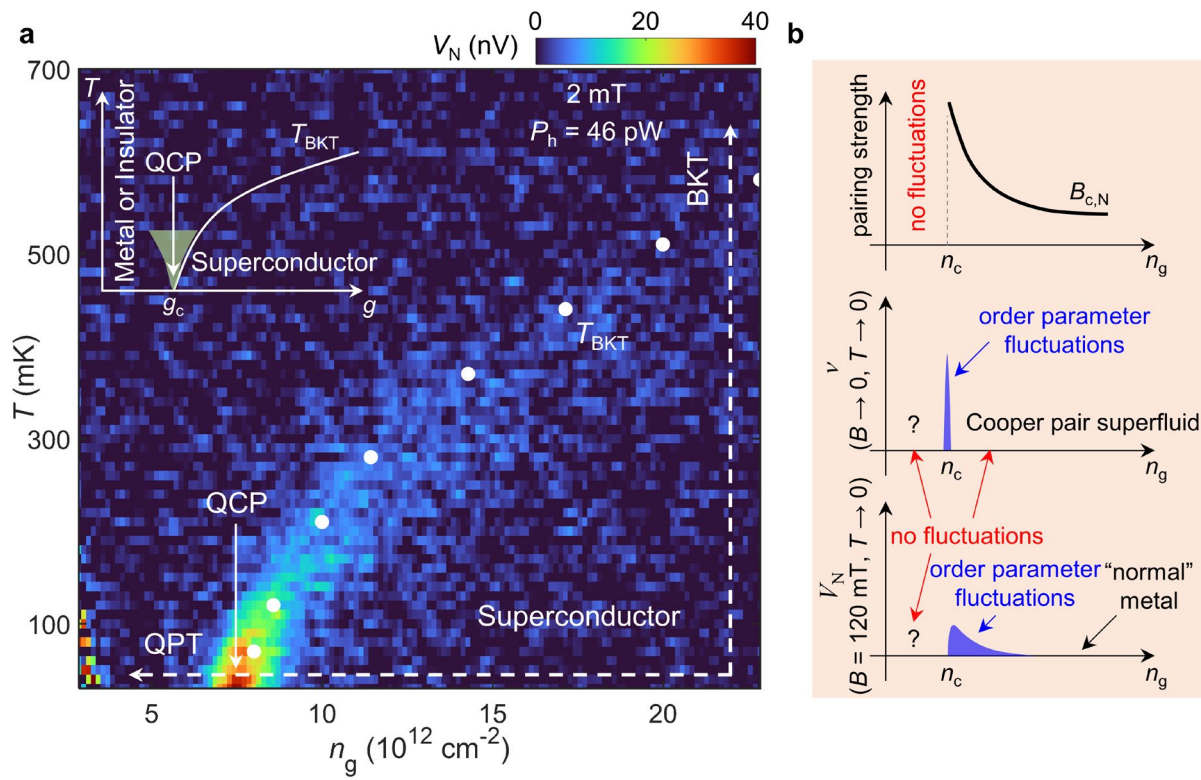


Fig. 4 | QPT and anomalous quantum fluctuations detected by Nernst effect. a, Nernst signal as a function of n_g and T . The white dots represent T_{BKT} . The inset sketches the typical phase diagram of a QPT, where the tuning parameter (g) is realized by n_g in our case. **b**, Illustrations of some key findings summarized from Figs. 2 and 3.

Methods

Device fabrication

The device fabrication process was separated into two parts: bottom and top, and followed closely to the previous reports^{9,10}. (i) Bottom: The hBN and graphite flakes were mechanically exfoliated onto 285 nm SiO₂/Si substrates and examined by optical and atomic force microscopy. Only atomically clean and smooth flakes with desirable thickness were used for making devices. The bottom hBN/graphite stacks were made using the standard dry transfer technique and released on SiO₂/Si substrates with pre-patterned Ti/Au (5/100 nm) metal pads for wire bonding. After dissolving the polymer in chloroform, Ti/Au (2/6 nm) electrodes and microheaters were deposited on top of the bottom stacks using standard electron beam lithography with a bilayer resist and electron beam evaporation. This was followed by another step of electron beam lithography and electron beam evaporation to deposit Ti/Au (5/60 nm) electrodes to connect the thin electrodes on the bottom stacks to the pre-patterned thick wire-bond metal pads. The surface of the electrodes on the stacks was finally cleaned using the contact mode of an atomic force microscope (AFM). (ii) Top: High-quality WTe₂ crystals were exfoliated onto 285 nm SiO₂/Si substrates in an inert gas (Argon) glovebox with water and oxygen concentration less than 0.1 ppm. Monolayer WTe₂ flakes were identified by optical contrast. The top graphite/hBN stacks were made using the same dry transfer technique. The monolayer WTe₂ flakes were then aligned with the top stacks and picked up. The top stacks were finally released on the bottom stacks, and the monolayer WTe₂ flakes were fully encapsulated and in contact with the bottom electrodes. The polymer was dissolved in chloroform for less than five minutes to minimize exposure to ambient conditions. The microscope and AFM images during the device 1 fabrication process are shown in Extended Data Fig. 1.

Electrical transport measurements

The devices were loaded into a dilution refrigerator equipped with a superconducting magnet and a base temperature of ~ 20 mK. Four-probe resistance measurements were performed using the standard AC lock-in technique with a frequency of ~ 13 Hz and an AC current excitation of ~ 5 nA.

Electron temperature calibration

The measurement wires in the dilution refrigerator are heavily filtered by Thermocoax cables. The electron temperature of the measurement condition was examined and calibrated⁴⁵ by the activation behavior of the fragile fractional quantum Hall states in an ultra-high mobility GaAs quantum well, i.e., $R_{xx} \propto \exp(-\Delta/2k_B T_e)$, where R_{xx} is the four-probe longitudinal resistance, Δ is the energy gap, k_B is the Boltzmann constant, and T_e is the electron temperature. Extended Data Fig. 2 shows R_{xx} in log scale versus the inverse fridge temperature ($1/T$), taken at the 14/9 fractional quantum Hall state. Below 45 mK, the electron temperature of the device deviates from the fridge temperature. We estimated the base electron temperature to be ~ 32 mK at a base fridge temperature of ~ 24 mK. Otherwise mentioned, the temperature mentioned throughout this paper refers to the electronic temperature.

Nernst measurements

The Nernst measurements were performed on the same devices in the same dilution refrigerator. As illustrated in Fig. 1a, the two microheaters were fabricated next to the monolayer WTe₂ flake, each being a thin narrow metal stripe (~ 200 nm wide and ~ 8 nm thick) with a low-temperature resistance of ~ 1 k Ω . We employed a dual-heater measurement scheme, and alternating current was applied to the two microheaters with the same frequency ($\omega \sim 13$ Hz), but a 90° phase shift between each other^{19–22}. This produced an alternating temperature gradient (∇T) while minimizing the change of the sample temperature itself near the measurement probes. The Nernst voltage drop (V_N) across the two probes is detected at the frequency of 2ω . The dual-heater power was as low as 46 pW in device 1 to generate ∇T and measure V_N , thanks to our vdW-heating device geometry. When the two microheaters were on, the sample temperature was expected to be a bit higher. At the base temperature of ~ 20 mK, when the two microheaters are supplied with a power of 46 pW, we estimate the local sample electron temperature of device 1 to be ~ 45 mK using the approach described below.

Temperature gradient estimation

Here we estimate the temperature gradient on monolayer WTe₂ generated by the microheaters. Instead of using external thermometers, we used the local two-probe resistance of monolayer WTe₂ itself to measure the in situ local temperature of the flake. This can be achieved because, at low carrier densities (the insulating state), monolayer WTe₂ exhibits a strong temperature-dependent resistance, making it a good thermometer.

As shown in Extended Data Fig. 3a, two pairs of probes (1 and 4 were chosen as Pair 1, 2' and 3' were chosen as Pair 2) near the Nernst probes (located in the middle) were selected to measure the local temperatures (T_1 and T_2). When Heater 1 is on and Heater 2 is off, a temperature difference is generated between Pair 1 and Pair 2, as illustrated in Extended Data Fig. 3b, and $T_1 > T_2$. Similarly, when Heater 1 is off and Heater 2 is on, the temperature gradient is reversed, and $T_1 < T_2$. Here, we show our procedure for estimating the temperature gradient when a DC current (I_h) is applied to Heater 2 while Heater 1 is off. Extended Data Figs. 3c and d show the two-probe resistance for Pair 2 and Pair 1, respectively, as a function of the Heater 2 current (I_h), at different fridge temperatures (T). The black dashed lines show the contour plots which trace the same R_{2p} , indicating the same local temperature of each pair. Following the black dashed line, a Heater 2 current can be tracked to a fridge temperature with both heaters off, which implies the local sample temperature near the pair. As a result, for a given Heater 2 power, a T_{2p} can be extracted for Pair 2 and Pair 1, respectively. Clearly, the heater power has a stronger effect on Pair 2 compared to Pair 1, because Heater 2 is closer to Pair 2. As an example, for the 100 pW power (DC current) at a fridge temperature (T) ~ 20 mK, the estimated local sample temperatures (T_1 and T_2) are ~ 120 mK and ~ 60 mK.

For the Nernst experiment, we employed a dual-heater measurement scheme and used the AC lock-in technique. Alternating current was applied simultaneously to the two microheaters with the same low frequency ($\omega \sim 13$ Hz), but a 90° phase shift between each other. The two currents are: $I_1 = I_h \sin(\omega t)$ and $I_2 = I_h \sin(\omega t + \frac{\pi}{2})$, and thus the powers are: $P_1 = \frac{1}{2} I_h^2 R_{h1} (1 - \cos(2\omega t))$ and $P_2 = \frac{1}{2} I_h^2 R_{h2} (1 + \cos(2\omega t))$, where R_{h1} and R_{h2} are the resistances of Heater 1

and Heater 2 ($\sim 1 \text{ k}\Omega$). This corresponds to an alternating temperature gradient, $\nabla T = \frac{\Delta T}{d} \sin(2\omega t - \frac{\pi}{2})$, where $\Delta T = (T_1 - T_2)$ is the extracted temperature difference and d is the distance between the two pairs which is $\sim 5.2 \text{ }\mu\text{m}$. The Nernst voltage drop (V_N) is detected at the frequency of 2ω with a crest factor ($\sqrt{2}$). The Nernst coefficient is defined as $\nu \equiv (E/B)/\nabla T$, where $E = \frac{V_N}{w}$ and w is the distance between the two probes which is $\sim 1.5 \text{ }\mu\text{m}$. For the 46 pW AC dual-heater power, the ∇T is estimated to be $\sim 5.3 \text{ mK}/\mu\text{m}$. For Fig. 3c, the corresponding Nernst coefficient is determined to be $\sim 4,100 \text{ }\mu\text{V}/\text{KT}$.

High efficiency of microheaters fabricated on vdW heterostructures

Here, we demonstrate that the location of the microheaters is key to measuring thermoelectricity of 2D crystals in a vdW stack. As shown in Extended Data Fig. 4a, we fabricated device 2 with a similar geometry to device 1 shown in the main text, but with additional microheaters located on and off the vdW stack. For a direct comparison, three microheaters are placed very close to each other, while Heater 1 is fabricated on top of both bottom hBN and graphite, Heater 2 is only in contact with bottom hBN, and Heater 3 is only in contact with SiO₂/Si substrate. Extended Data Fig. 4b shows the Nernst signal as a function of B measured using Heater 1 (red), Heater 2 (blue), and Heater 3 (black), respectively, using the same microheater power. One clear finding is that Heater 3 generates the smallest signal that can be barely detected. While Heater 2 generates a good signal, it is significantly lower compared to Heater 1. The data suggest that Heater 1 is most efficient in generating ∇T . This can be understood because at ultralow temperatures, graphite, as a metal, is a good thermal conductor. The idea here is to engineer the thermal path within the vdW stack, while avoiding the poor thermal path through SiO₂. We also intentionally chose the long and narrow rectangular graphite flake to enhance the uniformity of ∇T . In the experiments, the application of a heater power also raises the local temperature near the probe, in addition to generating ∇T . Hence to study QPT, the lowest possible heater power is preferred in order to minimize the sample temperature.

In device 1, we employ such a vdW-heating strategy and further optimize its performance by placing the heater very close to the monolayer sample. For device 2, this sample-heater distance is $\sim 20 \text{ }\mu\text{m}$, while in device 1 it is only $\sim 5 \text{ }\mu\text{m}$. As a result, we are able to generate efficiently a temperature gradient with an ultralow power ($\sim 46 \text{ pW}$), enabling the Nernst experiment on the monolayer sample down to the millikelvin regime.

Berezinskii–Kosterlitz–Thouless (BKT) transition temperature

Extended Data Fig. 6a shows the I - V curves in device 1 at various temperatures, which exhibit the characteristic nonlinear behaviors for a 2D superconductor. The black dashed line shows a tentative fit to the $V_{xx} \propto I_{DC}^3$ power law²⁶, which extracts T_{BKT} to be $\sim 580 \text{ mK}$ for $n_g = 22.84 \times 10^{12} \text{ cm}^{-2}$. The corresponding differential resistance (dV_{xx}/dI) as a function of I_{DC} and T is also shown in Extended Data Fig. 6b. Similarly, for various carrier densities, T_{BKT} is extracted by fitting to the $V_{xx} \propto I_{DC}^3$ power law and shown in Extended Data Fig. 6c.

Possible explanations for the sudden death of Nernst signals and the challenges

We first emphasize that, at this stage, our aim is to report the striking experimental findings rather than to identify the correct theory. While in the main text, we argue that the n_g -induced QCP is unconventional and requires an unusual explanation, here we provide further discussions on various possibilities in explaining the data, particularly regarding the sudden death of Nernst signals below the critical n_g .

The standard Landau-Ginzberg-Wilson (LGW) theory describes a continuous phase transition that connects an “ordered” phase (with a finite order parameter Δ) to a “disordered” phase ($\Delta = 0$). The LGW theory, therefore, doesn’t describe a direct continuous transition between two distinct ordered phases with different broken symmetries. The conventional way to think about a phase transition connecting two ordered phases includes (i) a first-order transition or (ii) two independent LGW transitions that are accidentally close to each other (namely, the transition in fact occurs in two steps, one from the ordered phase 1 to a disordered phase via an LGW transition and then the other from the disordered phase to the ordered phase 2 via another LGW transition). A single continuous phase transition that directly connects two ordered phases is beyond LGW theory, e.g., the theoretical proposals of deconfined QCPs (DQCPs)^{30–34}.

First, it is difficult to employ the scenario (i) of a first-order transition here since we are dealing with the superconductor to insulator/metal transition in a 2D system, in which a continuous phase transition, in particular, a BKT-like transition, is expected. A BKT-type phase transition is continuous. Experimentally, the detection of vortex Nernst signals provides strong support for the important role of vortices here, consistent with a BKT-like transition. We also find no evidence of any hysteresis in the transition, which speaks against a first-order transition. Second, the scenario (ii) is highly unusual as well since it involves two independent LGW transitions. In our observations, the n_g -tuned QCP at zero B is very sharp (Figs. 3a & b), i.e., the Nernst signal is sharply concentrated near a single critical density. Similarly, a sharp transition occurs in device 2 (Extended Data Fig. 7), even though the precise critical density differs between the two devices. It would be very unnatural to assume that within such a narrow regime, two independent LGW transitions occur. We hence deem these scenarios unlikely.

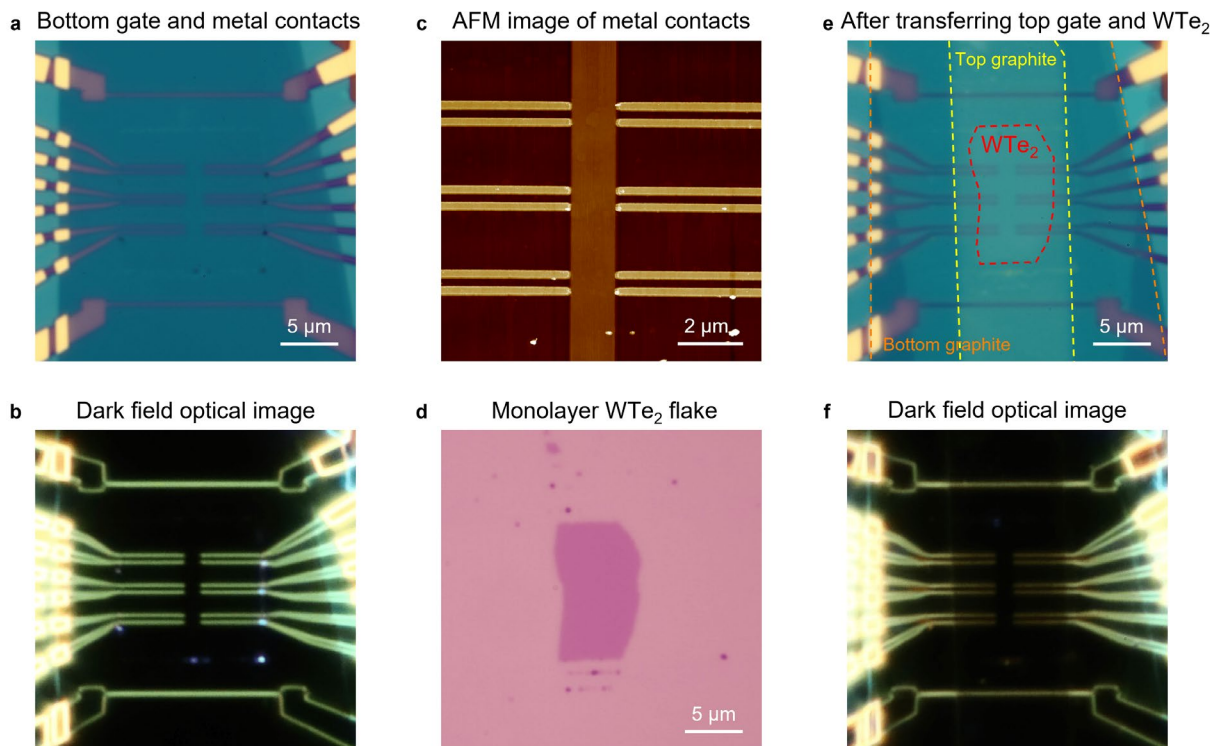
Next, we provide a brief discussion on the possibility of a DQCP, evaluating both the promises and challenges of this scenario. We summarize some key features of a DQCP^{30–34}. (a) The phase transition is continuous; (b) It separates two ordered phases (i.e., different spontaneous symmetry-breaking phases); and (c) Topological defects on one side (e.g., vortices in the superconducting state) proliferate at the transition, destroy the order, and then condense to form a new ordered phase on the other side. In the proposals of the doping-induced QSHI-to-superconductor transition^{32–34}, the topological defects are charged skyrmions on the QSHI side and vortices on the superconductor side.

Now we compare our experiments with these key DQCP features. (a) A superconductor-to-metal/insulator transition in 2D, such as the one that we are examining, is generically continuous. (b) The superconducting state above the critical doping n_c is surely ordered; the key is whether the non-superconducting side below n_c (i.e., regime III in Fig. 2a) is ordered or not. The sudden death of the Nernst signal may be regarded as a clue: it appears as if a new ordered phase is formed (an ordered phase suppresses fluctuations). If it were the usual “disordered” normal phase, fluctuations

would be present (e.g., like the normal state induced by B , above $B_{R,90\%}$). Another interesting observation is seen in Fig. 3b, in which very small B is applied so that the states on both sides of the n_g -tuned QCP are weakly perturbed. As shown in Fig. 3b and the inset, the fluctuations evolve from the asymmetric one at high B (e.g., ~ 10 mT, with a long tail on the superconducting side, unexpectedly) to a more symmetric one approaching zero B . The sharp concentration of the fluctuations at the QCP and the enhanced symmetry near zero B appear to indicate that the fluctuations below n_c are suppressed similarly to that on the ordered superconducting side. These observations seem to hint at the presence of a new ordered state below n_c . (c) Our Nernst experiments directly probe the topological defects on the superconducting side (i.e., the vortices). It is intriguing if one examines what happens to the Nernst signal at the lowest T and lowest B (Figs. 3a & b). In the superconducting state, no Nernst signal is detected (i.e., ordered, no fluctuations). When the n_g is reduced to the QPT, a dramatic Nernst signal rapidly develops, implying the proliferation of vortices. With a slight further decrease of n_g , however, the Nernst signal vanishes abruptly. Where do all the highly mobile vortices go? The data seem to imply that they transform into a new phase (regime III), which seems to be an ordered one based on the argument above in (b). All these unusual features are encouraging for exploring the possibility of a DQCP here. The theoretical proposals on the DQCP at a doping-induced superconducting transition from a spontaneous symmetry-breaking QSHI³²⁻³⁴ should further increase the interest in the QCP in monolayer WTe₂.

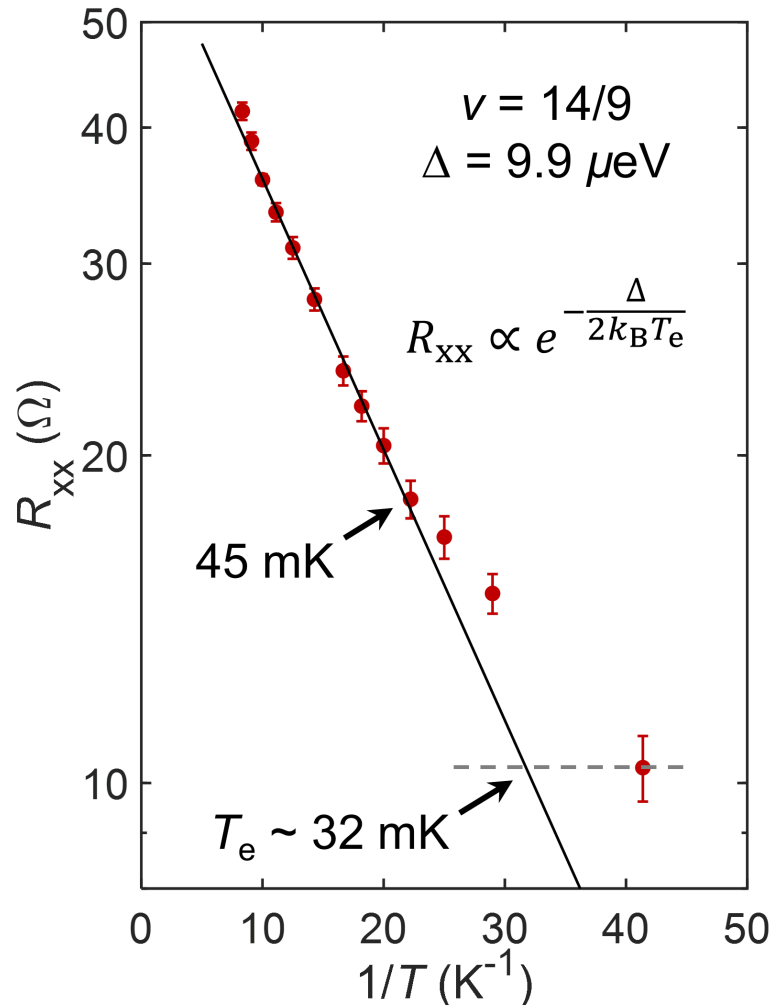
There are also challenges in employing the concept of DQCP here. (1) The presence of the metallic-like state (resistance $\sim k\Omega$, weakly temperature dependent) between the superconducting and the excitonic QSHI states challenges theoretical modelings. An anomalous metal state next to a superconducting state, even for a conventional QCP, is a challenging topic². We don't know how this state may alter the picture of a DQCP. (2) In the proposed DQCP in the QSHI-superconductor transition³², the QSHI order develops from spontaneous symmetry breaking. At the current stage, we don't know how this may happen in monolayer WTe₂. We note that the excitonic insulator state of the monolayer, which is formed spontaneously, may play a role. (3) Are there charged-2e skyrmions in regime III? Our experiments encourage the search for their presence in monolayer WTe₂. Their presence/absence is key to unlocking the secret. (4) The concept of DQCP is highly theoretical so far. Currently, a conclusive experimental demonstration of a DQCP remains absent and there exists no established standard for arguing which types of experimental data provide proof of this novel concept. In this regard, our results suggest that careful measurements of quantum fluctuations near the QCP can provide valuable guides to the theory. We hope our work motivates the development of concrete theoretical models examining quantum fluctuations near a DQCP or its alternatives. It is clear that a comprehensive understanding of the observed phenomena here and a clarification of its relations to the DQCP require substantial inputs from theory.

Extended Data Fig. 1



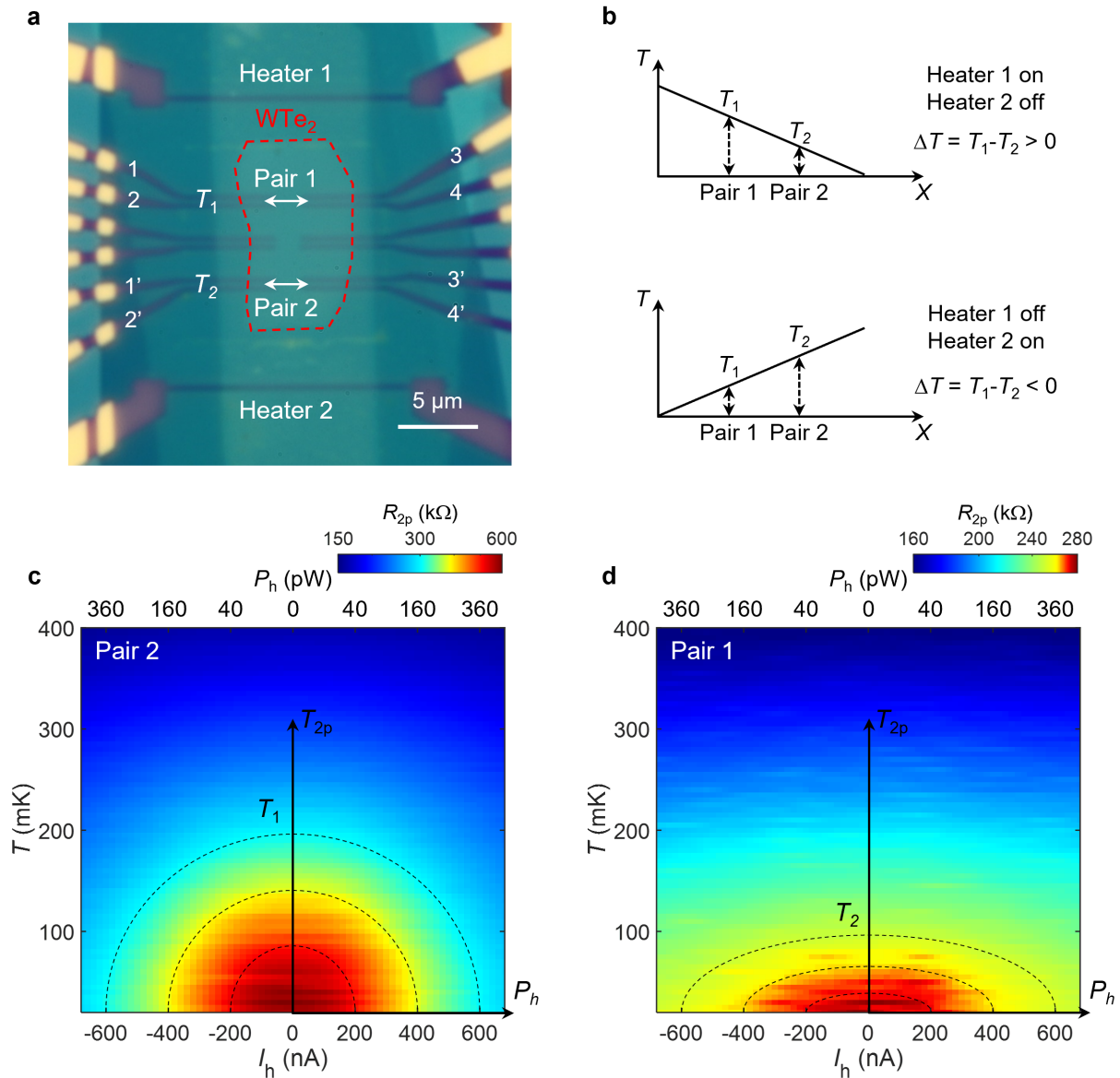
Extended Data Fig. 1 | Microscope and AFM images during the device 1 fabrication process. **a**, Bottom gate and metal electrodes after AFM tip clean. **b**, Dark field optical image of the bottom part. **c**, Tapping-mode AFM image of the metal electrodes. **d**, Microscope image of monolayer WTe_2 flake exfoliated in the glovebox. **e**, Microscope image of device 1 after transferring the top gate and monolayer WTe_2 . The monolayer WTe_2 flake is outlined in red. Top and bottom graphite flakes are outlined in yellow and orange. **f**, Dark field optical image of device 1. No bubbles were observed.

Extended Data Fig. 2



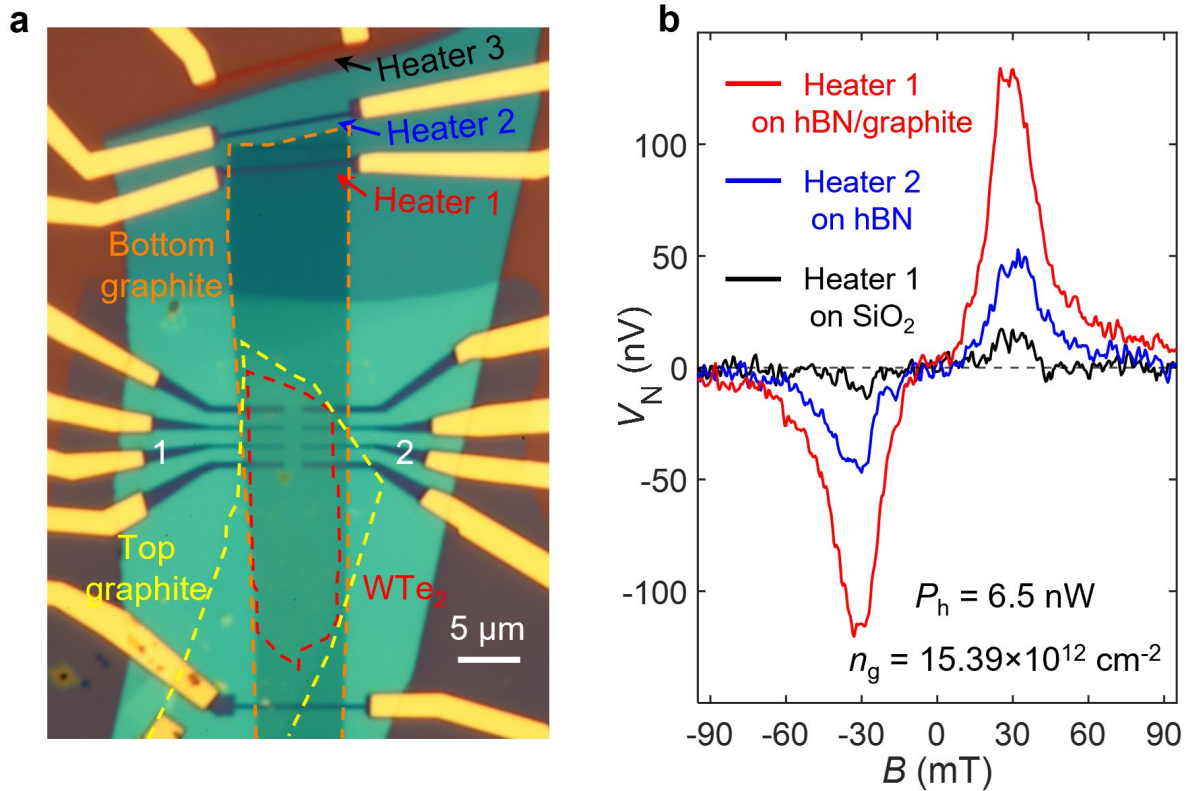
Extended Data Fig. 2 | Electron temperature calibration of the measurements in the dilution refrigerator. The calibration was performed based on an ultra-high mobility GaAs device with a series of fractional quantum Hall states. The plot shows the longitudinal resistance (R_{xx}) in log scale versus the inverse fridge temperature ($1/T$), taken at the $14/9$ fractional quantum Hall state.

Extended Data Fig. 3



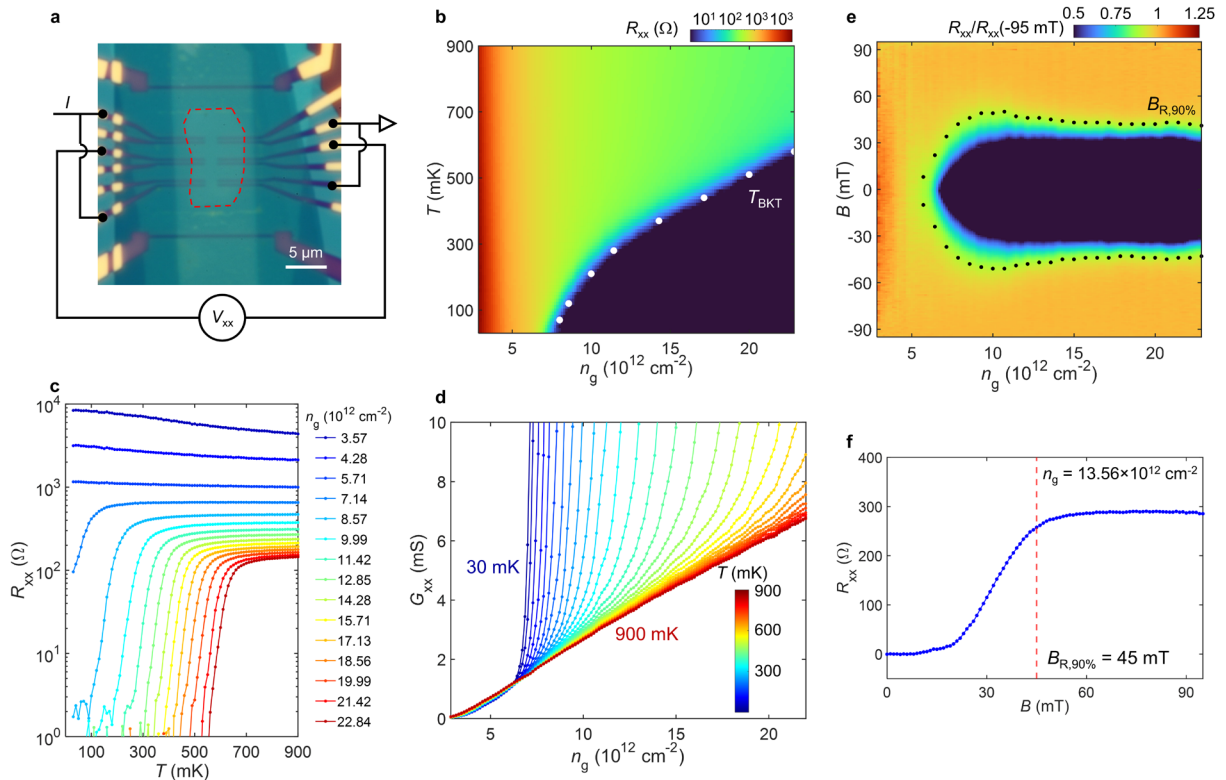
Extended Data Fig. 3 | Temperature gradient estimation in device 1. **a**, Microscope image of device 1 with the two-probe resistance measurement configuration. The monolayer WTe_2 flake is outlined in red. **b**, Temperature gradient generated by Heater 1 and Heater 2. **c** and **d**, Two-probe resistance for Pair 2 and Pair 1, respectively, as a function of the Heater 2 current and the fridge temperature. The black dashed lines trace the same R_{2p} , and extract T_1 and T_2 .

Extended Data Fig. 4



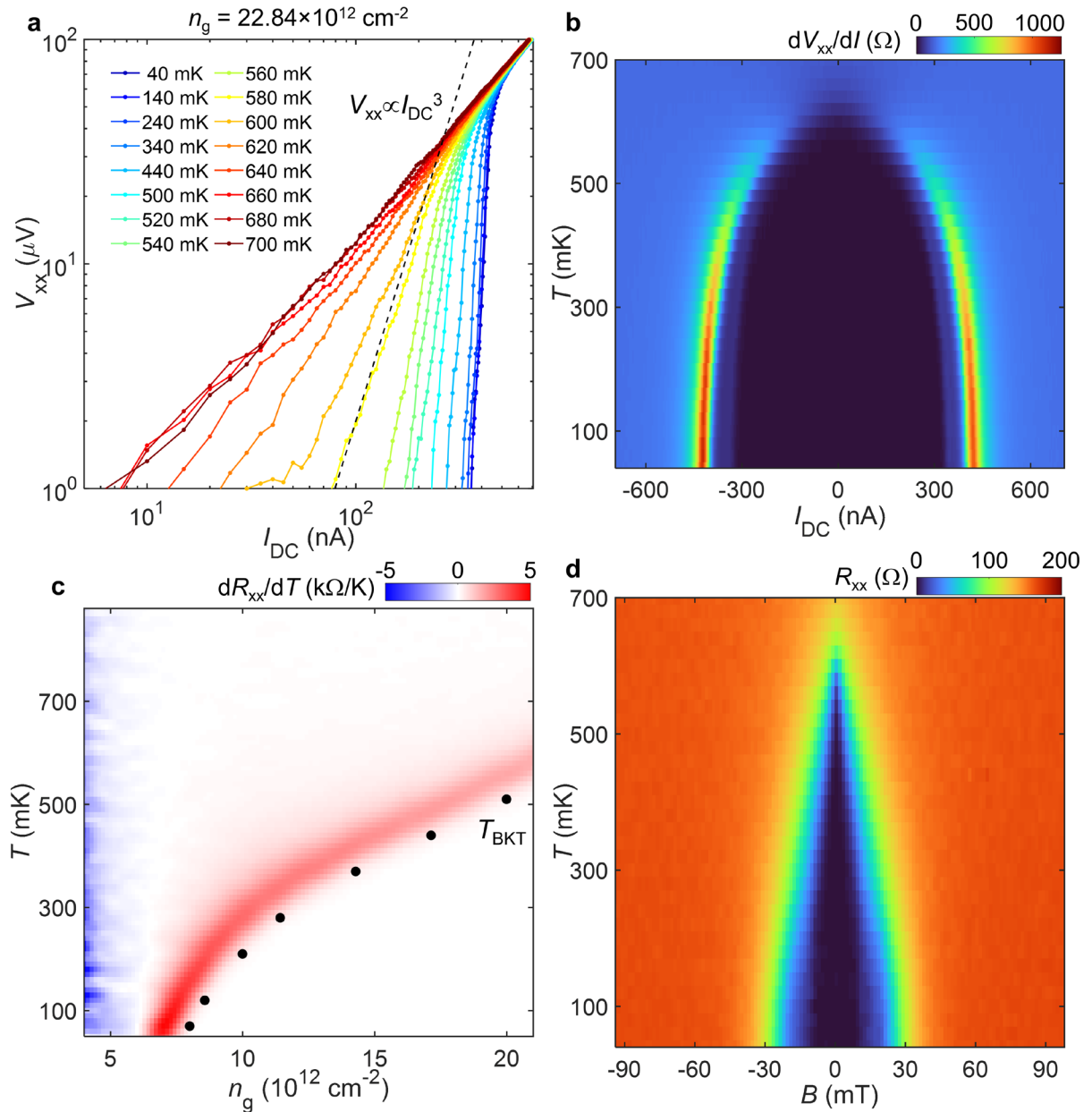
Extended Data Fig. 4 | High efficiency of microheaters fabricated on vdW heterostructures. **a**, Microscope image of device 2 with three microheaters fabricated on hBN/graphite (Heater 1), only hBN (Heater 2), and only SiO₂ (Heater 3), respectively. The monolayer WTe₂ flake is outlined in red. Top and bottom graphite flakes are outlined in yellow and orange. The Nernst signal was measured from the same two probes labeled 1 and 2. **b**, Nernst signal as a function of B measured with Heater 1 (red), Heater 2 (blue), and Heater 3 (black), respectively, for the same $P_h = 6.5$ nW and $n_g = 15.39 \times 10^{12}$ cm⁻².

Extended Data Fig. 5



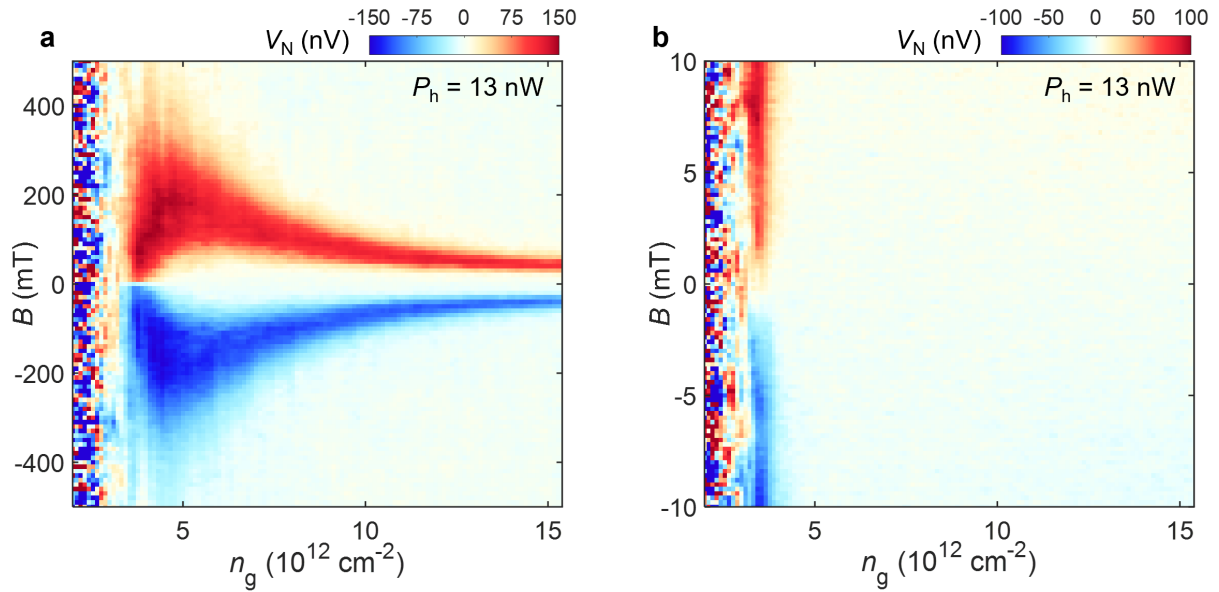
Extended Data Fig. 5 | Raw resistance data taken on device 1. **a**, Microscope image of device 1 with the four-probe resistance measurement configuration. The monolayer WTe_2 flake is outlined in red. **b**, Four-probe resistance as a function of n_g and temperature. The white dots represent T_{BKT} . **c**, Temperature dependence of R_{xx} for various n_g . **d**, The four-probe conductance (G_{xx}) calculated from R_{xx} as a function of n_g at various temperatures. **e**, Normalized R_{xx} as a function of n_g and B (the same data of Fig. 2b). For each n_g , R_{xx} is normalized to its value at -95 mT to highlight its B dependence. The black dotted line represents $B_{\text{R},90\%}$, at which R_{xx} drops to 90% of its saturated value at high B . **f**, R_{xx} as a function of B for $n_g = 13.56 \times 10^{12} \text{ cm}^{-2}$ showing a vertical line cut of **e**. The red dashed line indicates the identified $B_{\text{R},90\%}$.

Extended Data Fig. 6



Extended Data Fig. 6 | Extracting T_{BKT} in device 1. **a**, Characteristic nonlinear I - V curves on a logarithmic scale at various temperatures. The black dashed line shows a tentative fit to the $V_{xx} \propto I_{DC}^3$ power law, which extracts T_{BKT} to be ~ 580 mK for $n_g = 22.84 \times 10^{12} \text{ cm}^{-2}$. **b**, The corresponding differential resistance (dV_{xx}/dI) as a function of I_{DC} and T . **c**, dR_{xx}/dT as a function of n_g and T (the same data of Fig. 1b, using two neighboring points for the temperature derivative). The black dots represent T_{BKT} extracted by fitting to the $V_{xx} \propto I_{DC}^3$ power law for various n_g . **d**, B -dependence of R_{xx} as a function of T for $n_g = 22.84 \times 10^{12} \text{ cm}^{-2}$.

Extended Data Fig. 7



Extended Data Fig. 7 | Nernst data taken on device 2. **a**, Nernst signal as a function of n_g and B . **b**, Nernst signal as a function of n_g under very small B . The dual-heater power is 13 nW. The Nernst signal is recorded at the base temperature. The noise data (also seen in device 1) at low n_g is not antisymmetric to B and hence not Nernst signal. They likely arise due to bad contact to Au in this regime. The results reproduce the findings in device 1 discussed in the main text.